Simulations of naïve and KLA-activated macrophage plasma membrane models

Yueqi Niu[1], Si Jia Chen[2], and Jeffery B. Klauda[1,3*]

[1]Department of Chemical and Biomolecular Engineering, University of Maryland, College Park, MD 20742, USA

[2]Medical Scientist Training Program, Washington University in St. Louis School of Medicine, St. Louis, MO 63110, USA

[3]Institute for Physical Science and Technology, Biophysics Program, University of Maryland, College Park, MD 20742, USA

[*]Corresponding Author: jbklauda@umd.edu

Abstract

Macrophages (MAs), which play vital roles in human immune responses and lipid metabolisms, are implicated in the development and progression of atherosclerosis, a major contributor to cardiovascular diseases. Specifically, the abnormal lipid metabolism of oxidized low-density lipids (oxLDLs) in MAs is believed to be a crucial factor. However, the precise mechanism by which the MA membrane contributes to this altered lipid metabolism remains unclear. Lipidomic studies have revealed significant differences in membrane composition between various MA phenotypes. This study serves to provide and characterize complex realistic computational models for naïve (M0) and Kdo2-lipid A-activated (M1) state MA. Analyses of surface area per lipid (SA/lip), area compressibility modulus (K_A), carbon-hydrogen order parameter (S_{CH}), electron density profile (EDP), tilt angles, two-dimension radial distribution functions (2D RDFs), mean squared displacement (MSD), hydrogen bonds (H-bonds), lipid clustering, and lipid wobble were conducted for both models. Results indicate that the M1 state MA membrane is more tightly packed, with increased chain order across lipid species, and forms PSM-DOPG-CHOL and PSM-SLPC-CHOL clusters. Importantly, the bilayer thicknesses reported for the models are in good agreement with experimental data for the thicknesses of transmembrane regions for MA integral proteins. These findings validate the described models as physiologically accurate for future computational studies of MA membranes and their residing proteins.

1. Introduction

Macrophages (MAs) are important immune cells that protect the body against pathogens [1, 2]. Naïve macrophages can polarize into two phenotypes — the proinflammatory M1 and the anti-inflammatory M2 MAs. Surface proteins are important features that enable cell-cell and cell-substance interactions for these cells, triggering MA polarization and serving as markers for pathogen recognition by other immune cells [3, 4]. In addition to their contribution to immunity, MAs play a key role in lipid metabolism [5]. The uptake of oxidized low-density lipoprotein (oxLDL) by MA along the cardiovascular vessels leads to foam cell formation and, eventually, the development of atherosclerotic lesions. Interactions between oxLDL and CD36, a class B scavenger protein, would trigger the signaling cascades for oxLDL uptake by MA [6]. In addition, it is also indicated that CD36 is capable of transporting fatty acids through its internal tunnel [7]. However, the details of oxLDL uptake and the fatty acid uptake mechanism via CD36 are not fully understood.

Molecular dynamics (MD) simulations have been widely used to investigate the biophysical properties of target proteins, their substrates, and lipid bilayers with atomic resolution. Recent studies have utilized MD simulations to study the properties of immune cell plasma membrane proteins using homogeneous or near homogeneous phosphatidylcholine (PC) or phosphatidylethanolamine (PE) bilayers for simplicity [8-11]. While these studies have provided valuable insights into the targeted proteins, they may have undermined the contributions of membrane lipids to protein structures [12]. MAs are known to be a highly dynamic population that adapts to various environments, and their membrane lipid compositions can vary depending on their activation states [13, 14]. Using homogeneous bilayers in MD simulations for protein-bilayer systems may have overlooked several critical factors, including polar or non-polar interactions, lipid packing, and bilayer thicknesses, which can vary considerably depending on the membrane lipid composition. These variations can significantly impact the thickness of the transmembrane (TM) regions of membrane proteins and can potentially affect the adapted equilibrated protein conformation. Therefore, it is crucial to consider the membrane lipid composition when performing MD simulations of protein-bilayer systems to obtain a comprehensive understanding of their interactions.

MD simulations can offer valuable insights into protein-protein and protein-ligand interactions by employing bilayer models that mimic realistic lipid compositions. In this study, we seek to characterize two plasma membrane models of MA — the resting M0 state and the M1 state

induced by Kdo_2-lipid A (KLA) activation, based on Andreyev et al.'s lipidomic study [13]. We performed computational analyses of the models using approximately 500 ns of MD simulations for each state. Our results demonstrate that in order to gain a comprehensive understanding of the structure and functions of CD36 and other integral proteins on MAs through MD simulations, it is imperative to utilize bilayer models that accurately represent real-life lipid compositions due to the significant chemical and physical differences observed between the two proposed models, as well as between these models and the simple homogeneous models.

2. Methods

2.1 Model and System Setup

The models were constructed based on Andreyev et al.'s subcellular organelle lipidomic study, with data presented as the average lipid compositions of the two leaflets of membrane bilayers on RAW264.7 macrophages in the M0 and M1 states [13]. Asymmetric leaflet compositions are typical for cellular membranes. However, the models were not perfectly constructed and assumed symmetric leaflets due to the limited data availability. Despite this limitation, the models remained reasonable and were able to capture the most significant changes in bulk, providing valuable insights into lipid interactions within the plasma membrane of MAs.

Each modeled system consisted of 150 lipids per symmetric leaflet with compositions as detailed in Table 1. The initial composition selection for each model was based on headgroup abundance (Table S3). Within the chosen headgroup species, specific acyl chains were selected based on the degree of unsaturation, and the dominant lipids for each degree of unsaturation were selected in the models (Table S4). Comparing the compositions of the M0 and M1 models, while the headgroup selections remained unchanged, the lipid species and their respective numbers varied, reflecting previous findings that the lipidome of MA undergoes significant changes during different activation states, contributing to the differentiation into specialized populations [13, 14].

The *CHARMM-GUI Membrane Builder* was used to construct the bilayer systems. For each model, three independent bilayers with identical compositions were constructed in rectangular boxes with the compositions in Table 1 [15]. The bilayers were fully hydrated with at least 50 water molecules per lipid and neutralized with potassium counterions. At the time of building the M0 bilayers, the 1-eicosanoyl-2-octadecanoyl-*sn*-glycero-3-phosphocholine (EOPC) and plasmalogen phosphatidylethanolamine (20:4/18:0) (PLA20) topologies were not available on

CHARMM-GUI Membrane Builder. Therefore, 2,3 distearoyl-D-glycero-1-phosphatidylcholine (DSPC) and 1-stearoyl-2-arachidonyl-phosphatidylethanolamine (SAPE) were mutated to obtain EOPC and PLA20, respectively, with in-house lipid mutation code using the CHARMM program.

In the M0 model, a minor error occurred during the mutation of SAPE to PLA20 due to selection errors. As a result, the first and third replicates had 12 and 16 PLA20 on the top and bottom leaflets, respectively, while the second replicate had a symmetrical PLA20 distribution with 14 PLA20 on each leaflet. This led to asymmetrical SAPE and PLA20 distributions in two of the replicates. Despite this, our results indicate that this mistake had minimal impact on the bilayer behavior.

Table 1. Number of lipids of the M0 and M1 models per symmetric leaflet by lipid type[α,b]

	M0	M1	Δ Composition
CHOL	52	53	1.92%
EOPC (18:0/20:0)	5	—	—
DPPC (16:0/16:0)	—	5	—
SOPC (18:1/18:0)	10	12	20.00%
SLPC (18:2/18:0)	13	6	-53.58%
SOPE (18:1/18:0)	11	15	36.36%
SAPE (20:4/18:0)[b]	9	8	-11.11%
SOPS (18:1/18:0)	11	9	-18.18%
DSPS (18:0/18:0)	3	—	—
SLPS (18:2/18:0)	—	2	—
DOPG (18:1/18:1)	14	10	-28.57%
PLA20 (20:4/18:0)	14	11	-21.43%
PLA18 (18:1/18:0)	—	11	—
PSM	8	8	No Change

[α] CHOL: cholesterol;
EOPC: 1-eicosanoyl-2-octadecanoyl-*sn*-glycero-3-phosphocholine;
DPPC: 2,3 dipalmitoyl-D-glycero-1-phosphatidylcholine;
SOPC: 3-stearoyl-2-oleoyl-D-glycero-1-phosphatidylcholine;
SLPC: 1-stearoyl-2-linoleoyl-phosphatidylcholine;
SOPE: 1-stearoyl-2-oleoyl-phosphatidylethanolamine;
SAPE: 1-stearoyl-2-arachidonyl-phosphatidylethanolamine;
SOPS: 1-Stearoyl-2-Oleoyl-Phosphatidylserine;
DSPS: 2,3-distearoyl-D-glycero-1-Phosphatidylserine;
SLPS: 1-Stearoyl-2-Linoleoyl-Phosphatidylserine;
DOPG: 2,3-dioleoyl-D-glycero-1-phosphatidylglycerol;
PLA20: plasmalogen phosphatidylethanolamine (20:4/18:0);
PLA18: plasmalogen phosphatidylethanolamine (18:1/18:0);
PSM: palmitoylsphingomyelin.
[b] Final SAPE composition in each leaflet in the M0 model was not symmetrical (see methods).

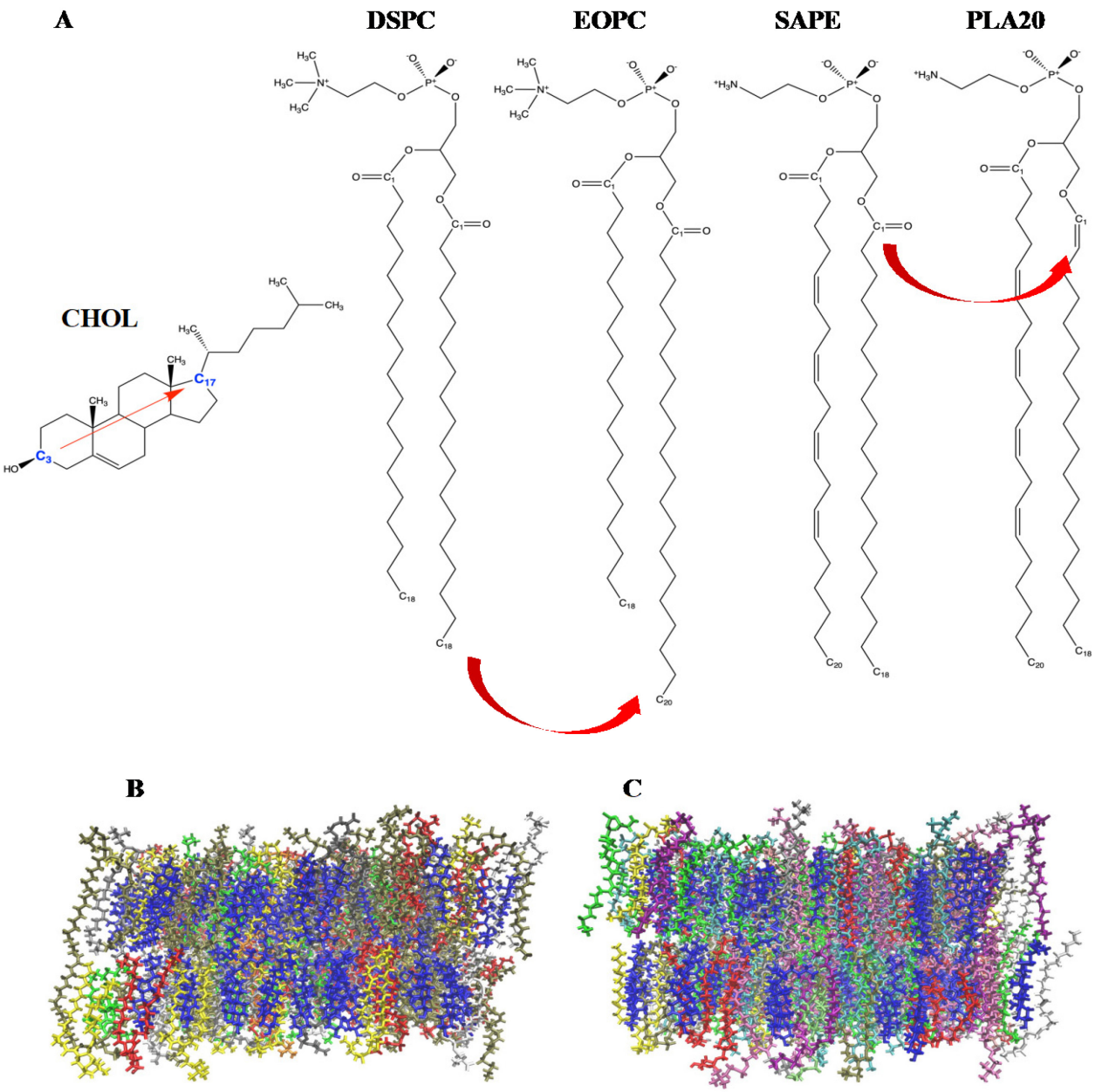

Figure 1. Key lipid structures and Bilayer Snapshots. A) The structure, reference atoms for tilt calculations (blue), and corresponding vectors (red) for CHOL, as well as the chemical structures of DSPC, EOPC, SAPE, and PLA20. The VMD snapshots of B) M0 macrophage model and C) M1 state macrophage model at the end of their corresponding simulation. Blue: CHOL; Red: DOPG; Grey: DSPS; Orange: EOPC; Yellow: PSM; Tan: SAPE; Silver: SLPC; Green: SOPE; White: SOPS; Pink: DPPC; Cyan: PLA18; Purple: PLA20; Lime: SLPS; Mauve: SOPC.

2.2 Simulation

The Nanoscale Molecular Dynamics (NAMD) program was used in combination with the CHARMM36 force field and TIP3 water model to carry out a standard *CHARMM-GUI Membrane Builder* six-step equilibration and the final production run [16-21]. Production runs for the M0 and M1 model systems were continued for 504 ns and 500 ns, respectively, with timesteps of 2 fs. The constant-pressure-constant-temperature (NPT) ensemble was used for all simulations. The physiological temperature of 310 K was maintained using Langevin dynamics while the constant pressure of 1 bar was maintained using Nosé-Hoover-Langevin piston [22, 23]. The Lennard-Jones potential was used to model the van der Waals interactions with a force-based switching function with interactions being switched off with a distance between 8 and 12 Å [20]. Long-range electrostatic interactions were calculated using the Particle Mesh Ewald (PME) fast Fourier transform with an interpolation order of 6 and a direct space tolerance of 10^{-6}.

2.3 Analysis

The properties of the M0 and M1 bilayer membranes were analyzed based on the last 250 ns of equilibrated simulation data as determined by equilibration analysis (Figure S1). The analyses conducted include the overall surface area per lipid (SA/lip), component SA/lip for each lipid type, area compressibility modulus (K_A), carbon-hydrogen order parameter (S_{CH}), electron density profile (EDP), tilt angles, two-dimension radial distribution functions (2D-RDFs), mean squared displacement (MSD), hydrogen bonds (H-bonds), lipid clustering, and lipid wobble. Statistical significance was determined by one-way ANOVA with at least $p < 0.05$ or by non-overlapping 95% confidence intervals.

To obtain the overall SA/lip, the area of the simulation box was divided by the number of lipids per leaflet. The component SA/lip was calculated using Quickhull [24]. Specifically, the *X* and *Y* coordinates of the representative atoms for each lipid were first obtained, with O3 for cholesterol, C2 for glycerol lipids, and C2S for sphingolipids. Using Quickhull, a Voronoi diagram was generated for each system, with each polygon representing a representative atom. Component SA/lip was obtained using the averaged sum of the areas of each representative atom for each lipid type. With overall SA/lip calculated, the K_A was calculated using the following formula:

$$K_A = \frac{k_B T \langle A \rangle}{N \sigma^2_{\langle A \rangle}} \quad (1)$$

where k_B, T, $\langle A \rangle$, N, and $\sigma_{\langle A \rangle}$ are the Boltzmann's constant, the absolute temperature, the average overall SA/lip, the number of lipids per leaflet, and the variance of the average SA/lip, respectively.

The carbon-hydrogen order parameters S_{CH} was calculated using the equation below:

$$S_{CH} = \left| < \frac{3}{2} cos^2\theta - \frac{1}{2} > \right| \quad (2)$$

where θ is the angle between the C-H bond vector and the bilayer normal. Tilt angle distributions were determined for cholesterol (CHOL). The tilt angle is defined as the angle formed between the bilayer normal and the vector connecting two representative atoms. The representative atom pairs used to calculate the tile angle for CHOL were C3-C17 (Figure 1A).

To obtain the EDPs, the bilayers were first repositioned to Z = 0 to obtain a symmetric top-bottom distribution. Electronic densities were then calculated for each atom and combined to get densities for each lipid and its corresponding functional groups. The EDPs were used to calculate the overall bilayer thickness (D_B), the headgroup-to-headgroup distance (D_{HH}), and the hydrophobic distance ($2D_C$). D_B, D_{HH}, and $2D_C$ were defined as the midpoint distance between the water EDPs, the distance between the peaks of the total EDPs, and the midpoint distance between the acryl chain EDPs, respectively.

The 2D-RDFs were calculated using the coordinates of the representative atoms of each lipid class: O3 for cholesterols, P for glycerol lipids, and NF for sphingolipids. MSD was calculated based on the average headgroup positions. Displacement was measured based on an individual lipid's position across time relative to its starting position. The number of H bonds formed, both inter- and intra-lipid, were calculated using CHARMM. A donor-acceptor pair was defined as having a distance less than 2.4 Å and a tilt angle greater than 150°.

Lipid clustering was examined using a Python scikit-learn package with the density-based spatial clustering of applications with noise (DBSCAN) algorithm [25, 26]. The cutoff distance used was 5.5 Å between headgroups for all lipids, and a cluster was defined as groups with at least three density-connected lipids.

The wobble or axial motions of the lipid were modeled using the correlation time of cross-chain vectors between C22 and C32 for glycerol phospholipids and C4S and C2F for sphingolipids. The second-rank reorientational correlational function is calculated for the cross-chain vectors using the following formula,

$$C_2(t) = \langle P_2[\hat{\mu}(0) \cdot \hat{\mu}(t)] \rangle \quad (4)$$

where $C_2(t)$, P_2, and $\hat{\mu}$ stands for correlational function, the second Legendre polynomial, and the cross-chain vector [27]. A two-exponential fit (n = 2) was then performed on $C_2(t)$ obtained from the mean of the three independent replicas, excluding the last 1/3 of output data truncated for time constants. The following custom fit equation was used in MATLAB to obtain the parameters,

$$C_2(t) = a_0 + \sum_{i=1}^{n} a_i e^{-\frac{t}{\tau_i}} \quad (4)$$

3. Results

3.1 Surface Area Per Lipid & Compressibility Modulus

The organization of lipid bilayer systems can be accessed using the overall SA/lip. By plotting the overall SA/lip against time, the state of equilibrium of the bilayers can be tracked. Both M0 and M1 models have reached equilibrium after 250 ns (Figure S1). The average overall SA/lipid and K_A were calculated and shown in Table 3.

Table 2. Key characteristics of the M0 and M1 models.

Model	M0	M1
Net charge	-28	-21
Anionic : Zwitterionic	1 : 3.5	1 : 4.62
% charged phospholipids	18.67	14.00
% saturated chains	41.84	47.42

Table 3. Average SA/lip and K_A for M0 and M1 MA model[α] and homogeneous POPC and POPE models [28]

Model	SA/lip ± SE (Å²)	K_A ± SE (N/m)
M0	47.06 ± 0.06	0.52 ± 0.03
M1	46.35 ± 0.07*	0.53 ± 0.04
POPC	66.00 ± 0.10	0.24 ± 0.01
POPE	58.70 ± 0.10	0.28 ± 0.02

[α]Errors are reported in standard errors (SE) obtained from the triplicates for each model.
*$p < 0.05$.

The K_A values for both models were statistically identical, but the overall SA/lip of the M1 model was significantly lower than that of the M0 model, indicating that the M1 model was more tightly packed. However, this difference was expected not to impact the K_A values significantly. It is well established that the amount of CHOL within bilayer systems would greatly impact these

two parameters. However, the CHOL content in each model was nearly identical, with CHOL accounting for 34.7% of the membrane composition for the M0 model and 35.3% for the M1 model, indicating that the change in SA/lip was likely not due to changes in CHOL behavior (Table 1). From the lipid composition per leaflet presented in Table 1, we observed an increase in net charge, a decrease in the percentage of charged phospholipids, and a decrease in the ratio of the number of the anionic to zwitterionic lipids in the M1 model when compared with the M0 model (Table 2). Further, we also found that the percentage of saturated chains increased from 41.84% in the M0 model to 47.42% in the M1 model (Table 2). These differences could contribute to the increase in lipid packing in the M1 model, revealing potential differences in lipid behaviors between the two models, as discussed later.

When the M0 and M1 models were compared with homogeneous POPC and POPE systems, the SA/lip was significantly lower in our built models with the corresponding higher K_A. This inverse relationship between SA/lip and K_A is expected since tighter-packed bilayers would require more force for compression. In contrast to the M0 and M1 models, the homogenous models lack the chemical diversity for energetically favored interactions based on headgroup polarity and hydrogen bonding capability, causing them to be more loosely packed.

Table 4. Component SA/lip for all lipids[α]

Lipid	M0 Area (Å^2) ± SE	M1 Area (Å^2) ± SE
CHOL*	28.77 ± 0.11	28.20 ± 0.03
PSM**	56.34 ± 0.46	51.31 ± 0.31
SOPC	57.80 ± 0.43	56.58 ± 0.17
SLPC	56.52 ± 0.25	56.29 ± 0.44
SOPE	56.22 ± 0.33	56.03 ± 0.26
SOPS*	57.25 ± 0.33	55.64 ± 0.04
DOPG**	58.56 ± 0.19	56.70 ± 0.21
PLA20	56.84 ± 1.02[b]	58.21 ± 0.20
SAPE**	53.38 ± 0.30[b]	57.06 ± 0.24
EOPC	57.21 ± 0.48	—
DSPS	56.07 ± 0.10	—
DPPC	—	55.63 ± 0.14
SLPS	—	55.69 ± 0.33
PLA18	—	57.51 ± 0.33

[α]Errors are reported in standard errors (SE) obtained from the triplicates for each model.
[b]This comes from replicas that have unequal distribution of SAPE (see methods).
P-values for the statistical test on area averages of M0 compared to M1 were listed for each lipid type and denoted with $^{*}p < 0.05$ and $^{**}p < 0.005$.

Since each lipid type has unique properties, component SA/lip was investigated to probe the difference in packing behavior in heterogeneous bilayers (Table 4). Even though the distributions of SAPE and PLA20 were asymmetric for the M0 model, the calculation for component SA/lip and any subsequent analyses were done by obtaining the averages of the top and bottom leaflets, minimizing the effect caused by the asymmetric distribution. The standard errors of SA/lip for all lipids, except PLA20, in the M0 model were comparable to those in the M1 model, demonstrating that the mutation error had resulted in little impact on the packing behavior in the M0 model, ensuring the accuracy and validity of the analyses below.

The vast majority of the common lipids across the two models have experienced a decrease in their corresponding SA/lip, which was in agreement with the observed decrease in the overall SA/lip above. One-way ANOVA test showed statistically significant decreases in the SA/lip for CHOL, PSM, SOPS, DOPG, and SAPE in the M1 model, indicating that these lipids have become more tightly packed and likely have experienced changes in their behaviors within the bilayer. The SA/lip of SAPE decreased significantly in the M1 model compared to that in the M0 model, while the SA/lip of CHOL, PSM, SOPS, and DOPG increased. Although the number of CHOL in the M1 model has increased slightly by 1.9%, its SA/lip has decreased significantly by 1.99%. PSM's composition remained constant across the two models, but its SA/lip of PSM decreased by 8.94% in the M1 model.

SOPC, SLPC, and SOPE have all experienced significant changes in composition in the two models, but their SA/lip remained statistically indifferent. In contrast, the compositions of SOPS and DOPG have changed drastically, with a significant decrease of 18.2% and 28.6%, respectively. In addition, SAPE has experienced a decrease in packing. While PLA20 also experienced the same pattern, its SA/lip values between the two models were found to be statistically insignificant due to the large SE found in the M0 model, likely caused by the asymmetric distribution.

3.2 C-H Order Parameters

The degree of order in lipid hydrophobic chains is determined using S_{CH}. A higher S_{CH} indicates a more ordered system with more ordered chains. Our findings supported the trend of decreasing S_{CH} with the presence of double bonds in a carbohydrate chain. Except for PSM, SAPE, and *sn*-1 chains of SOPC and SOPS, whose S_{CH} were statistically indifferent between the two models, all other chains were more ordered in the M1 model than the M0 model (Figure S2).

DOPG, SLPC, SOPE, and PLA20 have significantly increased chain orders in both *sn*-2 and *sn*-1 chains at C10-C14 and C4-C14, C4-C9 and C4-C16, C5-C14 and C11-C17, C15-C19 and C4-C12, respectively, for each lipid (Figure 2 & S3). The *sn*-2 chain of SOPC at C16-C17 and the *sn*-2 chain of SOPS at C12-C15 also show an increase in chain order (Figure 2 & S3). This global increase in chain order was likely due to the M1 model being more tightly packed.

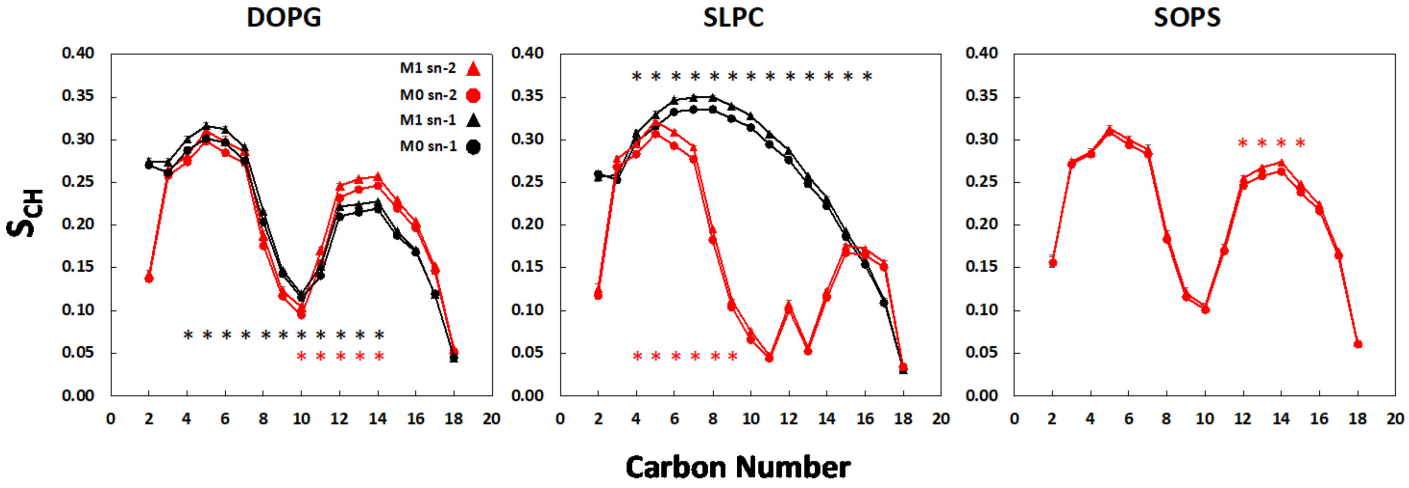

Figure 2. S_{CH}'s from DOPG, SLPC, and SOPS. $^{*}p < 0.05$.

3.3 Electron Density Profiles & Bilayer Thickness

The EDP is a measure of the electron probability distribution at being present at specific locations in the bilayer model. It provides information on the relative positions of the lipid headgroups with respect to the center of the membrane. Our results matched the expectation that if the number of a certain lipid species decreases, its corresponding electron density will decrease with no significant changes in peak patterns (Figure S5 & S6). Considering the average total EDP of both models, no significant differences were seen for the peak-to-peak distances, indicating that membrane thickness remained relatively constant across the two models (Figure S4A). This was confirmed by bilayer thickness calculations, which showed no significant differences in D_B, D_{HH}, and $2D_C$ between the two models (Table 5). While only CHOL and PSM showed slight increases

in their electron densities, no significant changes were observed for their peak distances, indicating no significant vertical movements (Figure S4).

Table 5. Calculated membrane thickness of the M0 and M1 macrophage models.

Model	D_{HH} (Å)	D_B (Å)	$2D_C$ (Å)
M0	46.73 ± 0.27	43.94 ± 0.04	35.55 ± 0.03
M1	46.47 ± 0.13	44.04 ± 0.10	35.69 ± 0.05

Furthermore, we found that the hydrophobic thicknesses of major MA transmembrane proteins from the Orientations of Proteins in Membranes (OPM) database largely agree with the $2D_C$ calculated for both M0 and M1 models, except for 2LNL, which has a lower than normal tilt angle of 19° (Table 6).

Table 6. PDB IDs and their reported hydrophobic thickness for transmembrane proteins commonly found on macrophages from the OPM database [29].

PDB ID	5T1A	6DO1	3V2Y	5O9H	3VW7	4IB4	2LNL
$2D_C$ (Å)	32.6	34.2	32.2	35.0	33.4	34.0	30.2

3.4 Cholesterol Tilt Analysis

The tilt modulus analysis examines the angle between the vector defined for the lipid and the lipid bilayer normal. The angles can provide insight into the spatial orientations of the lipid headgroups and acyl chains. A larger angle indicates that the vector is in a less upright position. CHOL is well known to form lipid rafts, which serve as the structural bases of many transmembrane proteins by forming a local environment that is highly ordered [30]. We found that the tilt angle of cholesterol is statistically indifferent between the two models, with both exhibiting the highest probability at a tilt angle of 11° (Figure S7).

3.5 Radial Distribution Function

2D-RDFs are used to determine the local arrangement of lipids within the bilayer system. It describes how the densities of a lipid vary as a function of distance from the lipid headgroup of interest. To investigate how lipid headgroups could influence lipid distributions within the bilayer, 2D-RDFs were generated between all lipid headgroup pairings in our systems (Figure S8 & S9).

Upon analysis, significant differences in the 2D-RDFs were observed for PSM, CHOL, DOPG, SLPC, SOPC, and SOPC.

In the M1 model, the first two peaks for DOPG-PSM 2D-RDF were stronger than those in the M0 model, and a leftward shift is observed for the third peak in the M1 model (Figure 4A). The DOPG-CHOL pair also shows significantly elevated peaks in the M1 model (Figure 4B). Similar to the DOPG-PSM 2D-RDF, both SLPC-PSM and SLPC-CHOL 2D-RDFs displayed increased peaks in the M1 model (Figure 4D & 4E). The self 2D-RDFs for both DOPG and SLPC showed a dramatic decrease, indicating that these lipids were likely shielded by other lipids in the M1 model (Figure 4C & 4F). The changes for SLPC were unexpected, as even when its composition in the M1 model was half that of the M0 model, significant increases in the 2D-RDFs were observed. In addition, compared to those in the M0 model, SLPC-DOPG 2D-RDF showed similar primary and secondary peaks but a decrease at the radius of ~15 Å before the elevation in the tertiary peak (Figure 4G).

It was expected that PSM and CHOL would be in closer proximity since they were laterally closer to DOPG and SLPC in the M1 model. As predicted, we observed a leftward shift in the third peak of the PSM self 2D-RDF at the radius of ~15 Å (Figure 4H). The CHOL self 2D-RDF also demonstrated a significant decrease in its primary peak in the M1 model (Figure 4I). Meanwhile, PSM-CHOL 2D-RDF exhibited reduced secondary and tertiary peaks (Figure S9). These changes in 2D-RDFs indicate that clusters involving PSM, DOPG, SLPC, and CHOL may have formed in the M1 model. The changes in the SLPC-DOPG 2D-RDF and the PSM self 2D-RDF suggest that either PSM is responsible for separating SLPC and DOPG within the cluster of all four lipids, or that SLPC and DOPG are clustered independently with CHOL and PSM.

Significant changes in 2D-RDF patterns were also observed for SOPC and SOPS between the two models, indicating an increased association between the two lipids. We observed a slightly elevated secondary peak and a leftward shift of the tertiary peak for SOPC-SOPS pairs (Figure 4J). Interestingly, the self 2D-RDFs for SOPS and SOPC exhibit similar changes but in opposite directions. SOPS self 2D-RDF showed an increase, while SOPC self 2D-RDF showed a decrease across the peaks (Figure 4K & 4L).

2D-RDFs were also sampled for the PE-CHOL pair and the DOPG-CHOL pair in blocks of 50 ns to ensure the representativeness of our observations in the M0 and M1 models (Figure S10). For both pairs in both models, the 2D-RDFs remained reasonably stable and demonstrated

little-to-no changes in local structure throughout the equilibrium time frame, indicating that our systems have converged and bilayers were fully relaxed.

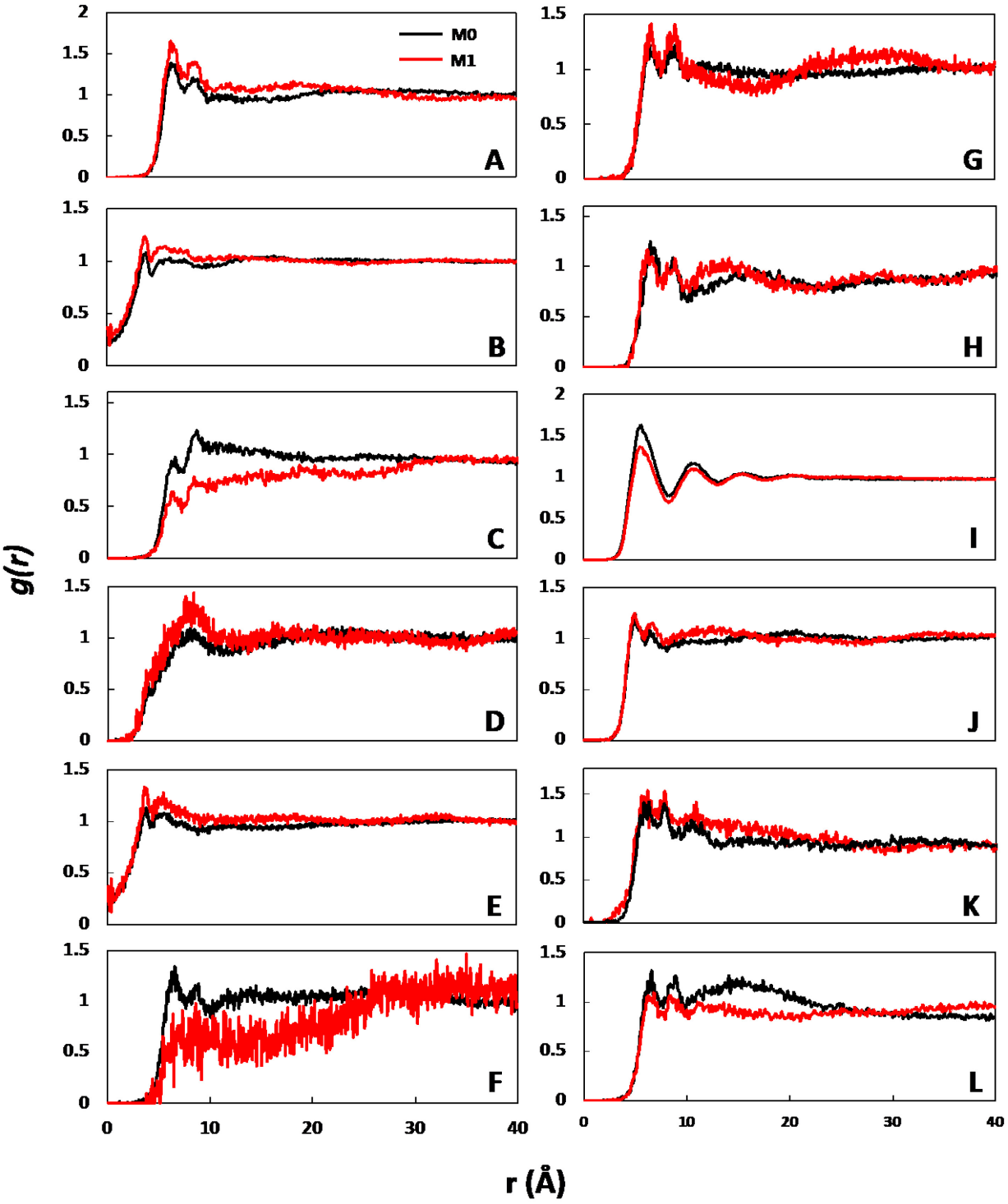

Figure 4. Selected 2D-RDFs for the M0 and M1 models. A) DOPG-PSM. B) DOPG-CHOL. C) DOPG-DOPG. D) SLPC-PSM. E) SLPC-CHOL. F) SLPC-SLPC. G) SLPC-DOPG. H) PSM-PSM. I) CHOL-CHOL. J) SOPC-SOPS. K) SOPS-SOPS. L) SOPC-SOPC.

3.6 Mean Squared Displacement

To further demonstrate that our bilayer systems were fully relaxed, an essential criterion for the lipid clustering analysis, MSD analysis was used to assess the lateral diffusion of the lipids in our bilayers. Albeit the caveats of the lateral diffusion coefficient (D_s) calculated in small systems due to the influence of periodic boundary conditions and the lack of long-range effects that allow for direct comparisons with experimental values, it remains appropriate to evaluate the membrane properties of our models. For all non-CHOL lipids, no statistically significant difference was found between D_s in the M0 and M1 models (Table 7). D_s calculated by lipid headgroup showed similar results (Table S5). However, this has further supported our observations that our bilayers were fully relaxed and reached equilibrium, ensuring that our systems were suitable for the subsequent lipid clustering analysis.

Table 7. Lateral diffusion coefficient (D_s) of all non-CHOL lipids in M0 and M1 models.

Model	M0	M1
D_s (cm^2/s)	$4.76 \times 10^{-8} \pm 5.56 \times 10^{-9}$	$4.70 \times 10^{-8} \pm 3.89 \times 10^{-8}$

3.7 Lipid Clustering

Studying lipid clusters could provide insight into the packing of lipids and can reveal details about headgroup interactions. In both models, we found that most clusters were formed with CHOL and PSM, while the fractions of other lipid types in clusters were lower than their overall composition. From the lipid clustering analysis, we found that the Rc-Rn values were statistically indifferent for most shared lipids between the two models. However, we observed significant increases in the Rc-Rn values of DOPG and SLPC, and significant decreases were observed for those of CHOL and PSM in the M1 model when compared to those for the M0 model, which matched the observations made for 2D-RDFs (Table 8).

Table 8. Differences between the fraction of the lipid in clusters (R_c) and the fraction of the lipid in the overall bilayer composition (R_n) for M0 and M1 models (R_c-R_n).

Lipids	M0 ± SE	M1± SE
CHOL**	0.046 ± 0.0016	0.031 ± 0.0014
DOPG***	-0.020 ± 0.0005	-0.012 ± 0.0006
PSM*	0.004 ± 0.0002	0.003 ± 0.0002
SLPC*	-0.007 ± 0.0013	-0.002 ± 0.0006
SOPC	-0.004 ± 0.0018	-0.004 ± 0.0014
SOPS	-0.002 ± 0.0007	0 ± 0.0013
SOPE	-0.003 ± 0.0012	-0.004 ± 0.0006
SAPE	-0.004 ± 0.0007	-0.003 ± 0.0004
PLA20	-0.005 ± 0.0015	-0.003 ± 0.0005

[α]Errors are reported in standard errors (SE) obtained from the triplicates for each model. Statistical comparisons between M0 and M1 were made, and significant differences were denoted with $^{*}p < 0.05$ $^{**}p < 0.005$ $^{***}p < 0.0005$.

348

349 The changes in R_c-R_n values for DOPG, CHOL, SLPC, and PSM support the speculation
350 that the clusters involving these lipids were present in the M1 model (Figure 5A & 5B). The
351 formation of clusters with CHOL and PSM caused an increase in R_c-R_n for DOPG and SLPC as
352 they were pulled in and had closer contact with CHOL and PSM. However, this also caused DOPG
353 and SLPC to be less associated with themselves, resulting in a decrease in their self 2D-RDFs. To
354 investigate whether the DOPG and SLPC were in the same clusters, we have visualized the clusters
355 (Figure 5). Upon examination, we found that DOPG and SLPC were in distinct clusters containing
356 PSM and CHOL. This observation led to our conclusion that while both lipids were clustered with
357 PSM and CHOL, DOPG and SLPC independently formed clusters with PSM and CHOL, with
358 little to no co-occurrence within CHOL and PSM-rich regions (Figure 5B). The formation of these
359 clusters has led to a more tightly packed bilayer, explaining the decrease in SA/lip, thus causing a
360 subsequent global increase in S_{CH}.
361 Interestingly, although the 2D-RDF results suggest an increased association between SOPS
362 and SOPC, no significant changes were observed in the clustering analysis. Upon further
363 investigation, it was found that most of the SOPC and SOPS were singled out and pushed out of
364 the clusters formed by other lipids, leading to their increased proximity and interactions with each
365 other (Figure 5C & 5D).

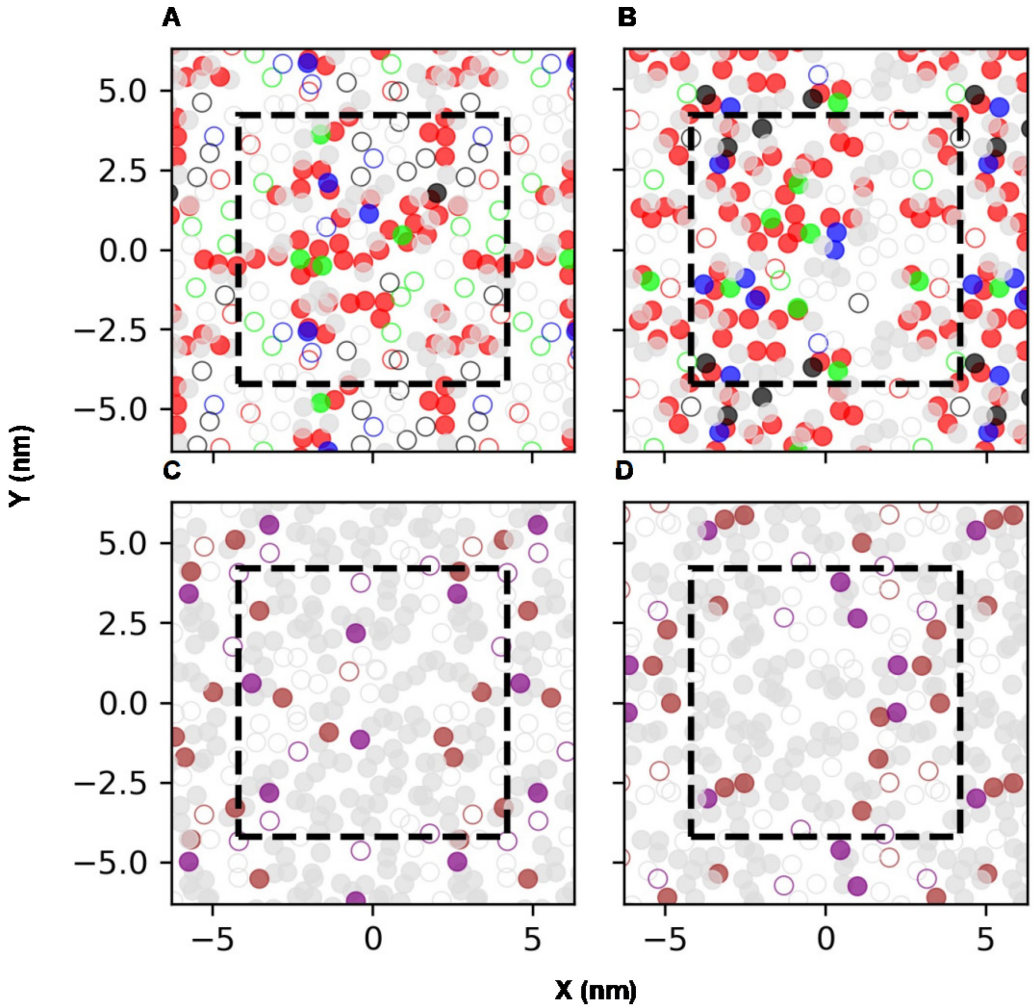

Figure 5. Visual representation of lipid clustering. Clusters involving PSM, DOPG, CHOL, and SLPC in the M0 **(A)** and M1 **(B)** bilayers. Clusters involving SOPC and SOPS in the M0 **(C)** and M1 **(D)** bilayers. Filled: in cluster; Unfilled: not in cluster; Red: CHOL; Green: DOPG; Blue: PSM; Black: SLPC; Purple: SOPS; Brown: SOPC; Grey: all other lipids.

3.8 Hydrogen Bonds

Hydrogen bonding plays a crucial role in determining the overall structural organization of bilayer systems. While intra-lipid H-bonding remained primarily unchanged between the two models (Figure S11), significant differences were observed in inter-lipid H-bonding, particularly for SOPC, PLA20, SAPE, SOPE, and SOPS. In the M1 model, a decrease in H-bonding per lipid with SLPC and DOPG as acceptors was observed for all five lipid types as donors when compared

to the M0 model. This decrease was likely due to the lower composition of SLPC and DOPG in the M1 model (Table 9).

The 2D-RDF and lipid clustering revealed the formation of clusters involving PSM, CHOL, DOPG, and SLPC in the M1 model. The H-bond results also suggest that PDM and CHOL shielded DOPG and SLPC. Despite the decrease in their compositions in the M1 model, no significant differences are observed for the number of H-bond per lipid formed with DOPG-DOPG, DOPG-PSM, SLPC-PSM, and SLPC-DOPG donor-acceptor pairs, indicating that SLPC and DOPG remained energetically favorable for forming such clusters with PSM and CHOL through H bonds.

Interestingly, a decrease in CHOL-DOPG donor-acceptor pairs was also observed, contrary to the expected increase with the increased proximity between the two. The decrease suggested that the role of CHOL in interaction with DOPG shifted away from being an H-bond donor. Additionally, a slight increase in H-bonding events was observed for DOPG-SOPE donor-acceptor pairs. This increase would contribute to the decrease observed for the SA/lip of DOPG. However, given that no other results suggested an increased association between the two, this increase in H-bonding could be due to coincidental placements of the two lipids in close proximity to each other during the membrane-building process using CHARMM.

The H-bond analysis provided insight into factors that contributed to the lowering of free energy and promoted the formation of energetically favorable clusters. In addition to the hydrophobic interactions between lipid chains and CHOL, the stabilizing factor for these clusters was found to be H-bonding events between DOPG, PSM, SLPC, and CHOL. The significant decreases in H-bonds per CHOL for DOPG and SLPC indicated that the primary role of CHOL in the M1 state bilayers was to provide structural integrity in the clusters. H-bonds form per lipid for PSM-CHOL donor-acceptor pairs also decreased slightly but with no statistical significance. A representative snapshot of the H-bonding formed within the PSM-DOPG-CHOL cluster was captured using VMD (Figure 6A). In this cluster, H-bonds were observed between O13 of PSM109 and HO3 of DOPG79, OF of PSM109 and HO2 of DOPG79, and OF of PSM109 and H3’ of CHOL102 (Figure 6D). A representative image was also captured for PSM-SLPC-CHOL clusters (Figure 6B). In this cluster, H-bonds were formed between O22 of SLPC60 and HNF of PSM48 (Figure 6E). Within these clusters, CHOL mainly served to provide structural integrity of the microdomains instead of being an H-bond donor.

The H-bond analysis revealed an increase in the overall H-bonds formed with SOPS in the M1 model despite a decrease in H-bond formations with DOPG and SLPC. This decrease was counterbalanced by increased H-bonding between the SOPC-SOPS donor-accepter pairs. Notably, the role of SOPS as an H-bond acceptor decreased as H-bonds formed between SOPE-SOPS and PLA20-SOPS donor-acceptor pairs decreased. Based on these observations, it could be inferred that clustering events would be observed for SOPC and SOPS. However, no significant differences were observed for their R_c-R_n values (Table 8). It was possible that during the formation of CHOL-DOPG-PSM clusters, SOPC and SOPS were displaced from the CHOL-rich clusters and into regions of the bilayer that were less ordered, leading to increased interactions between the two. A representative VMD snapshot of the SOPC and SOPS pair was obtained, and H-bonds identified between this pair were between HN3 of SOPS241 and O14 of SOPC201, as well as between HN1 of SOPS241 and O32 of SOPC201 (Figure 6C & 6F).

Table 9. Number of hydrogen bonds per lipid for lipids shared across the M0 and M1 model[α].

			Acceptors						
			SOPE	**SAPE[b]**	**PLA20[b]**	**SOPS**	**DOPG**	**PSM**	**SOPC**	**SLPC**
Donors	**SOPE**	M0	0.135 ± 0.017	0.040 ±0.003	**0.087* ±0.005**	**0.147* ± 0.017**	**0.147** ± 0.003**	0.016 ± 0.002	0.048 ± 0.002	**0.063* ± 0.007**
		M1	0.135 ±0.005	0.037 ±0.009	**0.055* ±0.006**	**0.093* ± 0.007**	**0.079** ± 0.009**	0.014 ± 0.003	0.057 ± 0.005	**0.029* ± 0.004**
	SAPE	M0	0.135 ± 0.010	0.118 ±0.004	0.078 ±0.006	0.135 ± 0.004	**0.142** ± 0.011**	0.018 ± 0.003	0.040 ± 0.006	**0.066* ± 0.006**
		M1	0.135 ± 0.016	0.111 ±0.009	0.066 ± 0.005	0.142 ± 0.018	**0.050** ± 0.004**	0.017 ± 0.005	0.057 ± 0.012	**0.026* ± 0.004**
	PLA20	M0	0.135 ± 0.002	0.049 ±0.001	0.156 ± 0.010	**0.136* ± 0.004**	**0.142** ± 0.005**	0.015 ± 0.000	0.050 ± 0.004	**0.066** ± 0.003**
		M1	0.135 ± 0.009	0.048 ±0.012	0.142 ± 0.006	**0.104* ± 0.014**	**0.063** ± 0.007**	0.011 ± 0.002	0.066 ± 0.004	**0.023** ± 0.009**
	SOPS	M0	0.079 ± 0.010	0.056 ±0.002	0.078 ± 0.010	0.196 ± 0.009	**0.103* ± 0.008**	0.007 0.002	**0.032* ± 0.002**	**0.048* ± 0.005**
		M1	0.078 ± 0.030	0.061 ±0.011	0.054 ± 0.016	0.192 ± 0.054	**0.046* ± 0.006**	0.006 ± 0.000	**0.048* ± 0.005**	**0.020* ± 0.009**
	DOPG	M0	**0.030* ± 0.002**	0.021 ± 0.001	0.031 ± 0.003	0.027 ± 0.003	0.514 ± 0.003	0.023 ± 0.000	0.029 ± 0.002	0.035 ± 0.007
		M1	**0.047* ± 0.003**	0.018 ±0.002	0.022 ± 0.004	0.026 ± 0.002	0.492 ± 0.010	0.022 ± 0.003	0.030 ± 0.004	0.018 ± 0.005
	PSM	M0	0.014 ± 0.007	± 0.014 ± 0.000	0.007 ± 0.005	0.037 ± 0.012	0.054 ± 0.009	0.563 ± 0.005	0.026 ± 0.003	0.043 ± 0.013
		M1	0.019 ± 0.003	0.014 ± 0.005	0.018 ± 0.003	0.021 ± 0.010	0.044 ± 0.011	0.570 ± 0.002	0.017 ± 0.006	0.034 ± 0.004
	CHL1	M0	**0.027** ± 0.002**	0.021 ± 0.001	**0.029* ± 0.002**	0.025 ± 0.001	**0.037** ± 0.000**	0.023 ± 0.002	0.025 ± 0.001	**0.032** ± 0.002**
		M1	**0.041** ± 0.003**	0.018 ± 0.004	**0.022* ± 0.005**	0.021 ± 0.012	**0.031** ± 0.003**	0.019 ± 0.002	0.031 ± 0.007	**0.018** ± 0.003**

[α]Errors are reported in standard errors (SE) obtained from the triplicates for each model.
[b]This comes from replicas that have unequal distribution of SAPE (see methods)
Statistical differences for M0 vs. M1 are denoted with $^{*}p < 0.05$ $^{**}p < 0.005$

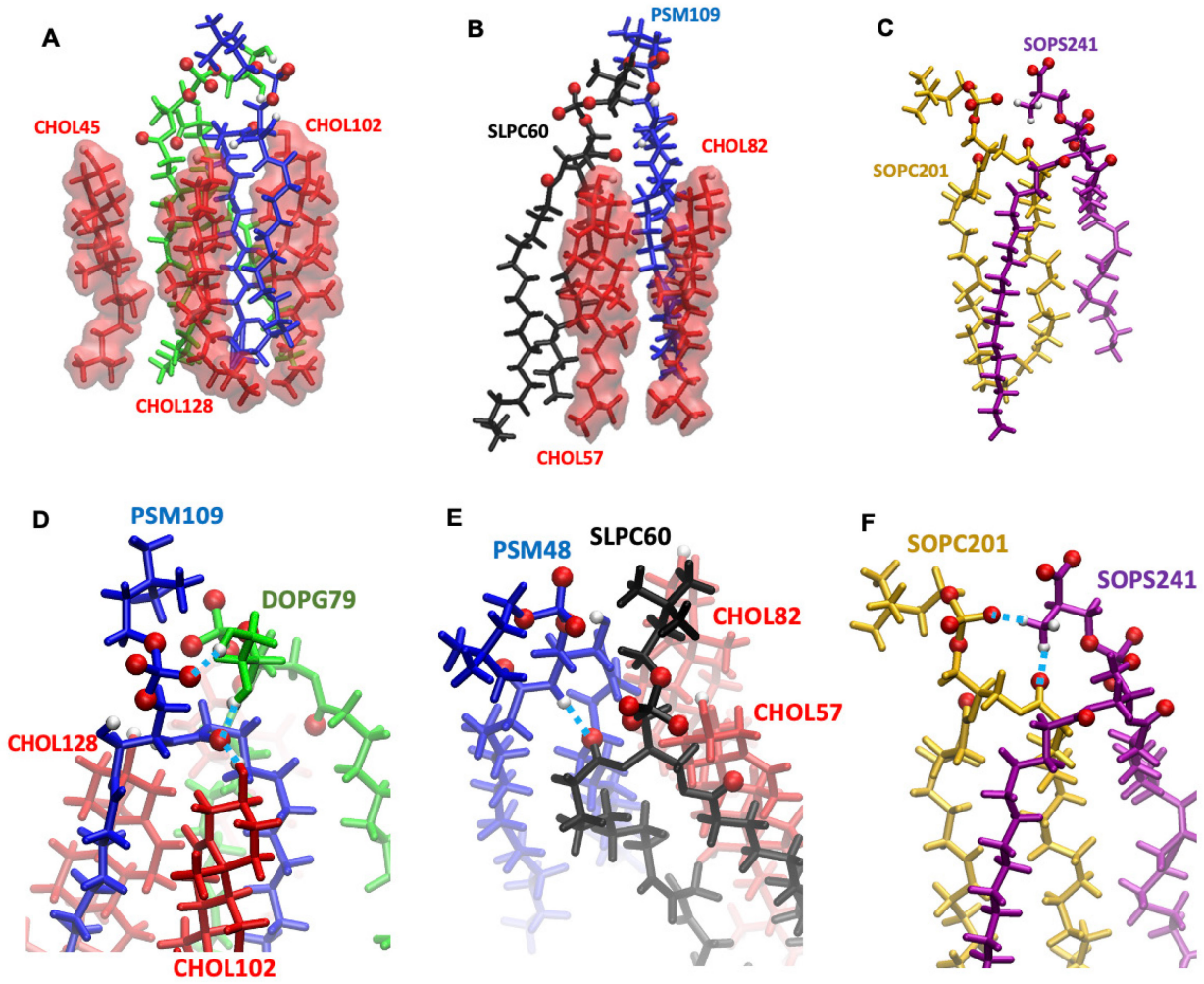

Figure 6. Representative VMD snapshots of the CHOL-DOPG-PSM cluster, the PSM-SLPC-CHOL clusters, and SOPC-SOPS pairs. **A)** Cluster of CHOL, PSM, and DOPG. **B)** Cluster of CHOL, PSM, and SLPC. **C)** SOPC and SOPS pair. Hydrogen bonds between **D)** PSM, DOPG, and CHOL in the cluster, **E)** PSM, SLPC, and CHOL in the cluster, and **F)** SOPC and SOPS pairs. Atoms with hydrogen bonding potential were shown in red for oxygen and white for hydrogen. Red: CHOL; Blue: PSM; Green: DOPG; Black: SLPC; Brown: SOPC; Purple: SOPS; Light blue dashes: hydrogen bonds.

3.9 Lipid Wobble Analysis

The lipid wobble analysis enables the investigation of lipid mobility by calculating the relaxation times for the cross-chain vectors. Using MATLAB, the correlation functions for all

glycerol lipids and individual lipids, including PSM, DOPG, and SOPE, were fitted to a second-order exponential function (Figure S12 & S13). The relaxation times obtained from the fits were reported (Table 10). Given the timescale of the study, although the fast relaxation times (τ_1) captured some trend, the intermediate relaxation times (τ_2) are of greater interest for analysis.

Table 10. Average values and 95% confidence levels (CL) of the second-order exponential fit to correlation functions of the cross-chain vector of the upper carbons for all glycerol lipids, PSM, DOPG, and SOPE[α].

Relaxation Time (ns)	Model	Glycerol Lipids	Lipid		
			PSM	DOPG	SOPE
		Average 95% CI	Average 95% CI	Average 95% CI	Average 95% CI
τ_1	M0	0.8275 (0.8018, 0.8532)	**2.791*** (2.615, 2.967)	**0.8256*** (0.7932, 0.8581)	**0.1876*** (0.1806, 0.1927)
	M1	0.8599 (0.8307, 0.8890)	**1.402*** (1.291, 1.513)	**0.6548*** (0.6227, 0.6869)	**0.94*** (0.8851, 0.9949)
τ_2	M0	14.05 (13.92, 14.19)	**29.67*** (29.10, 30.24)	**14.14*** (13.97, 14.31)	15.03 (14.59, 15.47)
	M1	14.1 (13.94, 14.25)	**25.28*** (24.86, 25.70)	**13.52*** (13.36, 13.69)	15.2 (14.89, 15.51)

[α]Errors are reported in standard errors (SE) obtained from the triplicates for each model.
* Non-overlapping 95% CL for M0 vs. M1

The relaxation times for all glycerol lipids and sphingolipids were assessed separately due to differences in atom naming in CHARMM topology. As glycerol lipids were dominant in both M0 and M1 models, the relaxation times of the glycerol lipids in these models may serve as an approximate value for overall bilayer relaxation times. Statistical analysis revealed no significant difference between the bilayer relaxation times of the two models.

However, statistical differences were found for individual lipids. Although no significant differences are observed in SOPE, a control lipid, between the M0 and M1 models, the τ_2 of PSM and DOPG were significantly decreased in the M1 model. In the M1 model, PSM and CHOL were found to form clusters with DOPG. As PSM and DOPG were present in clusters where lipid mobility was limited and acyl chain movements were restrained, their relaxation times became shorter.

4. Discussion

In this study, we have observed significant differences in the chemical and physical properties of MA plasma membranes between M0 and M1 states, indicating that changes in plasma membrane composition play an important role in modulating MA functions under various conditions.

4.1 The need for realistic models

The orientation of transmembrane regions of integral proteins can be influenced by the tilt angles of CHOL, which is not considered in homogeneous lipid bilayer models. It has been shown that for DPPC systems, the inclusion of sterols, such as CHOL and ergosterol, can significantly affect the tilt angle of sterols in a concentration-dependent manner and subsequently impact the chain tilt and chain order of neighboring DPPC lipids [31]. Therefore, simple homogeneous or heterogeneous glycerol phospholipid models may not fully capture the structural and functional detailed interactions between the membrane and the transmembrane regions of proteins. Moreover, in the context of MAs, many crucial proteins, such as those involved in cytokine recognition, inflammatory activation, and substance transportation, are localized in CHOL-rich lipid rafts [32-34]. Thus, CHOL should be included in the lipid systems used for protein docking studies to better understand macrophage integral proteins using computational methods. As computational power advances and bilayer models grow in complexity, representing the composition of realistic membranes, the bilayers used for *in silico* studies would closely mimic membrane behaviors under *in* vitro, in *vivo*, or *ex vivo* conditions.

In addition, realistic membrane models would benefit *in silico* studies on lipid-protein interactions and have a broader implication for studies investigating the biological appropriateness of bioengineered exogenous agents. Luo et al. used MD simulations to probe the potential interactions between two-dimensional (2D) nanomaterials and MA plasma membranes with homogeneous POPC bilayers [35]. Later, improved from the homogeneous PC model, Gu et al. employed a more realistic human monocyte bilayer that lacks chain diversity to investigate the molecular mechanism of PEGylated molybdenum disulfide-induced macrophage immune response [36]. The trend of applying realistic membrane models in *in silico* studies has stressed the need for realistic cell type- and state-specific bilayer models to better probe the mechanistic details of the interactions of interest. This has further demonstrated the importance of this work in

providing a starting point for those who aim to study and compare interactions across MA phenotypes.

4.2 Validity of our models

As Silva Filho et al. and Chakraborty et al. had examined, MAs possess negative surface charges regardless of their phenotype [37, 38]. At the same time, the activated MAs should have a more negative surface charge than the naïve MAs. Similarly, in our models constructed based on the lipidomic analysis for M0 and M1 MAs by Andreyev et al., both our M0 and M1 models have net negative charges (Table 2). However, the charge for the M0 model was more negative than the M1 model. At first glance, this might conflict with the published literature. A clear distinction of what contributes to the negative surface charge is needed in this case. Upon further examination, the net negative surface charges of MAs and the changes in surface charges observed for activated MAs are contributed mainly by the changes in the number of sialic acid residues on the plasma membrane and by the changes in the electrostatic distribution on the extracellular regions of MA surface proteins [37, 38]. Montenegro Burke et al. and Morgan et al. both profiled the lipids of MAs under different states. However, both studies employed a bulk approach and did not isolate and analyze the lipid profile of each cell organelle [39, 40]. Andreyev et al.'s lipidomic study that this work is based on remains to be the only study available that has conducted a thorough and detailed profiling of lipids present in different organelles of M0 and M1 state RAW 256.9 cells, a common MA cell line of mouse origin [13]. Therefore, whether the lipid composition on plasma membranes of MAs contributes to the changes in the net surface charge remains unclear due to the lack of available literature investigating the lipid compositions of various cell compartments of MAs. Nevertheless, Andreyev et al. have presented one possibility that the lipids did not play a significant role in contributing to the negative surface charges but contributed by assisting the assembly of proteins with negative surface charges and presenting negatively charged residues on MA surfaces.

One well-known feature of plasma membranes is the lipid composition asymmetry between the intra- and extracellular leaflets. Verkleij et al. were one of the first to put forward this concept, where they found that more SM and PC lipids were found on the extracellular leaflet, more PE lipids were located on the intracellular leaflet, and PS lipids were almost exclusively present in the intracellular leaflet [41]. Our proposed M0 and M1 MA plasma membrane models were constructed

based on the assumption that bilayers have symmetric lipid composition. With this assumption, one might question whether the observations made from the clustering analysis have any biological significance. PG lipids, while being a major lipid on bacterial membranes, only comprise 1-2% of phospholipids found in mammalian cells [42]. Because PG is a minority anionic lipid, little is known about its distributions on the two leaflets. While negatively charged lipids tend to reside on the intracellular leaflet, SM and CHOL are present in both leaflets. Therefore, our observation of clusters involving DOPG, PSM, and CHOL represents a possibility that PG might play some role in facilitating the functions of the M1 state MAs.

A comparative study done by van Duyl et al. has demonstrated that CHOL has a greater tendency to interact with sphingolipids than with phospholipids, revealing the role of CHOL-PSM interactions in the context of lipid rafts [43]. The study is supported by Lönnfors et al., which demonstrated that sterols, specifically CHOL, have a higher affinity for sphingolipids than phospholipids when bilayers contain only CHOL and SM or CHOL and PC, while no significant differences were reported for bilayer acyl-chain orders in these systems [44]. These findings are further supported by Bera et al.'s *in silico* study, which demonstrated that the introduction of POPC or POPE into systems containing PSM and CHOL resulted in decreased lipid axial relaxation time and increased formation of PSM-CHOL clusters [45]. It suggested that the decreased relaxation time was due to the preferential interaction between CHOL and PSM. In our models with diverse lipid profiles, we observed that the relaxation times for PSM in both models have further decreased to around 30 ns, whereas systems containing only PSM or PSM and CHOL would have relaxation times that are approximately 3-5 times higher depending on their relative concentrations and system temperature.

In sum, the observations made for our models are in agreement with findings from relevant *in vitro* and *in silico* studies. With the evidence drawn from the similarity found between the hydrophobic thicknesses of our models and the common MA integral proteins, it is reasonable to conclude that our proposed models are biologically representative and suitable for future *in silico* studies.

4.3 Applicability of our models

MAs are known to be highly diverse, consisting of many subsets. Previous studies have shown that the sensitivity of these subsets towards the inflammatory environment can be

influenced by the internalization of exogenous lipids and incorporation of these lipids into macrophage plasma membranes [40, 46-48]. It can be inferred that such modification would further promote macrophage subset differentiation and change the sensitivity of the cells to a local environment through alterations in lipid compositions on the plasma membrane. Such alterations would most likely impact the composition of the lipid rafts, where important proteins of macrophages are reported to be located [32-34]. In our study, we probed the presence of lipid rafts through the lipid clustering analysis on a nanometer scale. After KLA activation of M0 MAs, we observed an increase in clusters involving DOPG or SLPC with PSM and CHOL when they entered the M1 state for proinflammatory actions. Because of the increased DOPG involvement, the clusters formed were more negative in the M1 state than those in the M0 state. Together, our observations suggested that these lipids might play a role in regulating the M1 subsets by constructing local environments that are energetically favorable for certain transmembrane proteins.

Previous research by Rubio et al. has demonstrated that ethanolamine plasmalogens are important for facilitating MA phagocytosis [49]. The findings showed that MAs with plasmalogen deficiency exhibited reduced phagocytic activity, but when supplemented with exogenous plasmalogen, their phagocytic activity was significantly improved, along with increased lipid raft formation. The lipidomic study conducted by Andreyev et al. showed that the KLA-activated M1 state macrophage has increased ether-linked phospholipids, particularly the ether-linked phosphatidyl ethanolamine subclass [13]. However, the clustering analysis for our models did not observe increased clustering for PLA20, partly due to the asymmetric distribution of PLA20 in the M0 model. The three phenotypes of MA demonstrate various levels of phagocytic activities, with M2 MAs having the highest phagocytic activity, M1 MAs possessing a modest phagocytic activity, and M0 MAs being the least active in phagocytosis [50-52]. Therefore, it may be challenging to observe the contribution of plasmalogens to lipid clustering when comparing M0 and M1 state MAs. Nonetheless, West et al. have validated the plasmalogen force field parameters in CHARMM36 all-atom force field for PLA18 and have demonstrated that the incorporation of plasmalogens into POPC bilayers increases bilayer thickness and tail orders, indicating the ability of plasmalogens to contribute to lipid clustering [19].

Furthermore, Petkevicius et al. have previously reported a linkage between PC metabolism and pro-inflammation activation of MAs [53]. In particular, MAs deficient in the rate-limiting

enzyme in the *de novo* PC biosynthesis pathway, phosphocholine cytidylyltransferase A (CCTα), have shown decreased membrane PC turnover and significantly reduced proinflammatory activity in response to palmitate, highlighting the critical role of PC in the proinflammatory actions of MAs. Our findings showed an increase in clusters involving PSM, SLPC, and CHOL, even when the number of SLPC in the M1 model was reduced to half of that in the M0 model. This observation underscores the importance of such microdomains and indirectly supports the role of PC metabolism in guiding the proinflammatory actions of macrophages.

Gaus et al. conducted a study investigating the lipid profiles of the raft and non-raft regions on the MA plasma membrane of THP-1 cells, a human-origin monocyte cell line [54]. They have observed more SM lipids present in raft regions and non-raft regions. Further, authors have found that SM contents are still higher in raft regions for cells treated with sphingomyelinase, partially depleting the SM content on membranes. In summary, our observations of clusters involving PSM match the observations made *in vivo*, further supporting the applicability of our models.

4.4 Future directions

One important aspect of our model that is in need of improvement is the consideration of the asymmetry of our bilayers. The differential lipid composition between the intra- and extracellular leaflets could serve important functions and provide important indicators of cell conditions. Our proposed models were constructed based on the assumption that the bilayers have symmetric leaflets due to the limited data available on the lipid profiles of the MA plasma membrane by leaflet. Further, the limited data availability has grounded our work to compare only between M0 and M1 state MAs, excluding the anti-inflammatory M2 state MA. This calls for future lipidomic studies on plasma membranes of the different states of mouse-derived MA cell lines, human-origin MA cell lines, or primary human monocytes. These studies profiling the plasma membrane of MAs in various states and detailing the asymmetry of their membranes could significantly improve our understanding of this subject and facilitate the development of accurate plasma membrane models of future *in silico* research involving MAs.

In this work, the term “realistic” is narrowly defined where the composition of the bilayer models mirrors that of living cells, and these bilayers should possess similar properties to the plasma membranes of living cells. Homogeneous PC or PE bilayers are the most commonly used for protein structural-functional *in silico* studies. As demonstrated in this work, this approach has

overlooked the physical and chemical diversities of membrane lipids. It is reasonable to conclude that potential lipid-protein interactions that might be important for protein anchoring or functioning remain understudied. Future work should aim to broaden the definition of "realistic" so that these dynamic cellular events can be produced and studied in such *in silico* models. Beyond constructing realistic bilayer models based on lipidomes available, we shall seek applications of such models with the incorporation of membrane proteins to mimic the actual membrane environments. The continuous improvements of force fields and developments in computational algorithms would further facilitate the efforts to mirror what happens in living cells in a computational space, with the potential to reveal key interactions and help identify novel targets for therapeutics.

5. Conclusion

The M0 and M1 models in this study represent a step toward developing accurate MA membrane models. More complex models are needed to accurately reflect the bilayer properties, including but not limited to membrane asymmetry, lipid flip-flop, and incorporation of membrane proteins. Additionally, given the dynamic nature of MAs, distinct MA subsets may exhibit unique bilayer features that are currently beyond our ability to model. Nonetheless, considering the support from previous *in vitro* and *in silico* studies, our models are reasonably physiologically accurate and can serve as a basis for future computational studies investigating the characteristics of the MA plasma membrane and its integral proteins.

6. Acknowledgments

The high-performance computing clusters used for this study are Deepthought2 and Zaratan maintained by the Division of Information Technology at the University of Maryland. This work was in part supported by NSF (MCB-1951425 and CHE2003912). Si Jia Chen was supported by the NIH Medical Scientist Training Program (NIH/NIGMS T32GM007200). Model structures of the membranes discussed in this work can be obtained using the following link: https://terpcnnect.umd.edu/~jbklauda/memb.html.

7. References

(1) Murray, P. J.; Wynn, T. A. Protective and pathogenic functions of macrophage subsets. *Nat Rev Immunol* **2011**, *11* (11), 723-737. DOI: 10.1038/nri3073 From NLM.

(2) Elhelu, M. A. The role of macrophages in immunology. *J Natl Med Assoc* **1983**, *75* (3), 314-317. From NLM.

(3) Taylor, P. R.; Martinez-Pomares, L.; Stacey, M.; Lin, H. H.; Brown, G. D.; Gordon, S. Macrophage receptors and immune recognition. *Annu Rev Immunol* **2005**, *23*, 901-944. DOI: 10.1146/annurev.immunol.23.021704.115816 From NLM.

(4) Slomianny, M. C.; Dupont, A.; Bouanou, F.; Beseme, O.; Guihot, A. L.; Amouyel, P.; Michalski, J. C.; Pinet, F. Profiling of membrane proteins from human macrophages: comparison of two approaches. *Proteomics* **2006**, *6* (8), 2365-2375. DOI: 10.1002/pmic.200500546 From NLM.

(5) Noy, R.; Pollard, J. W. Tumor-associated macrophages: from mechanisms to therapy. *Immunity* **2014**, *41* (1), 49-61. DOI: 10.1016/j.immuni.2014.06.010 From NLM.

(6) Park, Y. M. CD36, a scavenger receptor implicated in atherosclerosis. *Exp Mol Med* **2014**, *46* (6), e99. From NLM.

(7) Akachar, J.; Etchebest, C.; El Jaoudi, R.; Ibrahimi, A. The computational analyses, molecular dynamics of fatty-acid transport mechanism to the CD36 receptor. *Sci Rep* **2021**, *11* (1), 23207. DOI: 10.1038/s41598-021-01373-5 From NLM.

(8) Alba, J.; Rienzo, L. D.; Milanetti, E.; Acuto, O.; D'Abramo, M. Molecular Dynamics Simulations Reveal Canonical Conformations in Different pMHC/TCR Interactions. *Cells* **2020**, *9* (4). DOI: 10.3390/cells9040942 From NLM.

(9) Triantaphyllopoulos, K. A.; Baltoumas, F. A.; Hamodrakas, S. J. Structural characterization and molecular dynamics simulations of the caprine and bovine solute carrier family 11 A1 (SLC11A1). *J Comput Aided Mol Des* **2019**, *33* (2), 265-285. DOI: 10.1007/s10822-018-0179-x From NLM.

(10) Ray, A. G.; Choudhury, K. R.; Chakraborty, S.; Chakravarty, D.; Chander, V.; Jana, B.; Siddiqui, K. N.; Bandyopadhyay, A. Novel Mechanism of Cholesterol Transport by ABCA5 in Macrophages and Its Role in Dyslipidemia. *J Mol Biol* **2020**, *432* (17), 4922-4941. DOI: 10.1016/j.jmb.2020.07.006 From NLM.

(11) Krishnan, S.; Liu, F.; Abrol, R.; Hodges, J.; Goddard, W. A., 3rd; Prasadarao, N. V. The interaction of N-glycans in Fcγ receptor I α-chain with Escherichia coli K1 outer membrane protein A for entry into macrophages: experimental and computational analysis. *J Biol Chem* **2014**, *289* (45), 30937-30949. DOI: 10.1074/jbc.M114.599407 From NLM.

(12) Bogdanov, M.; Mileykovskaya, E.; Dowhan, W. Lipids in the assembly of membrane proteins and organization of protein supercomplexes: implications for lipid-linked disorders. *Subcell Biochem* **2008**, *49*, 197-239. From NLM.

(13) Andreyev, A. Y.; Fahy, E.; Guan, Z.; Kelly, S.; Li, X.; McDonald, J. G.; Milne, S.; Myers, D.; Park, H.; Ryan, A.; et al. Subcellular organelle lipidomics in TLR-4-activated macrophages. *J Lipid Res* **2010**, *51* (9), 2785-2797. DOI: 10.1194/jlr.M008748 From NLM.

(14) Dennis, E. A.; Deems, R. A.; Harkewicz, R.; Quehenberger, O.; Brown, H. A.; Milne, S. B.; Myers, D. S.; Glass, C. K.; Hardiman, G.; Reichart, D.; et al. A mouse macrophage lipidome. *J Biol Chem* **2010**, *285* (51), 39976-39985. DOI: 10.1074/jbc.M110.182915 From NLM.

(15) Jo, S.; Kim, T.; Iyer, V. G.; Im, W. CHARMM-GUI: a web-based graphical user interface for CHARMM. *J Comput Chem* **2008**, *29* (11), 1859-1865. DOI: 10.1002/jcc.20945 From NLM.

(16) Phillips, J. C.; Braun, R.; Wang, W.; Gumbart, J.; Tajkhorshid, E.; Villa, E.; Chipot, C.; Skeel, R. D.; Kalé, L.; Schulten, K. Scalable molecular dynamics with NAMD. *J Comput Chem* **2005**, *26* (16), 1781-1802. DOI: 10.1002/jcc.20289 From NLM.
(17) Klauda, J. B.; Venable, R. M.; Freites, J. A.; O'Connor, J. W.; Tobias, D. J.; Mondragon-Ramirez, C.; Vorobyov, I.; MacKerell, A. D., Jr.; Pastor, R. W. Update of the CHARMM all-atom additive force field for lipids: validation on six lipid types. *J Phys Chem B* **2010**, *114* (23), 7830-7843. DOI: 10.1021/jp101759q From NLM.
(18) Venable, R. M.; Sodt, A. J.; Rogaski, B.; Rui, H.; Hatcher, E.; MacKerell, A. D., Jr.; Pastor, R. W.; Klauda, J. B. CHARMM all-atom additive force field for sphingomyelin: elucidation of hydrogen bonding and of positive curvature. *Biophys J* **2014**, *107* (1), 134-145. DOI: 10.1016/j.bpj.2014.05.034 From NLM.
(19) West, A.; Zoni, V.; Teague, W. E., Jr.; Leonard, A. N.; Vanni, S.; Gawrisch, K.; Tristram-Nagle, S.; Sachs, J. N.; Klauda, J. B. How Do Ethanolamine Plasmalogens Contribute to Order and Structure of Neurological Membranes? *J Phys Chem B* **2020**, *124* (5), 828-839. From NLM.
(20) Jorgensen, W. L.; Chandrasekhar, J.; Madura, J. D.; Impey, R. W.; Klein, M. L. Comparison of simple potential functions for simulating liquid water. *The Journal of Chemical Physics* **1983**, *79* (2), 926-935. DOI: 10.1063/1.445869.
(21) Durell, S. R. a. B. B. R. a. B.-N. A. Solvent-Induced Forces between Two Hydrophilic Groups. *The Journal of Physical Chemistry* **1994**, *98* (8), 2198-2202. DOI: 10.1021/j100059a038.
(22) Martyna, G. J.; Tobias, D. J.; Klein, M. L. Constant pressure molecular dynamics algorithms. *The Journal of Chemical Physics* **1994**, *101* (5), 4177-4189. DOI: 10.1063/1.467468.
(23) Feller, D.; Glendening, E. D.; Woon, D. E.; Feyereisen, M. W. An extended basis set ab initio study of alkali metal cation–water clusters. *The Journal of Chemical Physics* **1995**, *103* (9), 3526-3542. DOI: 10.1063/1.470237.
(24) Barber, C. B.; Dobkin, D. P.; Huhdanpaa, H. The quickhull algorithm for convex hulls. *ACM Trans. Math. Softw.* **1996**, *22* (4), 469–483. DOI: 10.1145/235815.235821.
(25) Ester, M.; Kriegel, H.-P.; Sander, J.; Xu, X. A density-based algorithm for discovering clusters in large spatial databases with noise. In Proceedings of the Second International Conference on Knowledge Discovery and Data Mining, Portland, Oregon; 1996.
(26) Pedregosa, F.; Varoquaux, G.; Gramfort, A.; Michel, V.; Thirion, B.; Grisel, O.; Blondel, M.; Prettenhofer, P.; Weiss, R.; Dubourg, V.; et al. Scikit-learn: Machine Learning in Python. *J. Mach. Learn. Res.* **2011**, *12* (null), 2825–2830.
(27) Klauda, J. B.; Roberts, M. F.; Redfield, A. G.; Brooks, B. R.; Pastor, R. W. Rotation of lipids in membranes: molecular dynamics simulation, 31P spin-lattice relaxation, and rigid-body dynamics. *Biophys J* **2008**, *94* (8), 3074-3083. From NLM.
(28) Yu, Y.; Klauda, J. B. Update of the CHARMM36 United Atom Chain Model for Hydrocarbons and Phospholipids. *J Phys Chem B* **2020**, *124* (31), 6797-6812. DOI: 10.1021/acs.jpcb.0c04795 From NLM.
(29) Lomize, M. A.; Lomize, A. L.; Pogozheva, I. D.; Mosberg, H. I. OPM: orientations of proteins in membranes database. *Bioinformatics* **2006**, *22* (5), 623-625. DOI: 10.1093/bioinformatics/btk023 From NLM.
(30) Simons, K.; Toomre, D. Lipid rafts and signal transduction. *Nat Rev Mol Cell Biol* **2000**, *1* (1), 31-39. DOI: 10.1038/35036052 From NLM.
(31) Alavizargar, A.; Keller, F.; Wedlich-Söldner, R.; Heuer, A. Effect of Cholesterol Versus Ergosterol on DPPC Bilayer Properties: Insights from Atomistic Simulations. *J Phys Chem B* **2021**, *125* (28), 7679-7690. DOI: 10.1021/acs.jpcb.1c03528 From NLM.

(32) Fallahi-Sichani, M.; Linderman, J. J. Lipid raft-mediated regulation of G-protein coupled receptor signaling by ligands which influence receptor dimerization: a computational study. *PLoS One* **2009**, *4* (8), e6604. From NLM.
(33) D'Aprile, C.; Prioni, S.; Mauri, L.; Prinetti, A.; Grassi, S. Lipid rafts as platforms for sphingosine 1-phosphate metabolism and signalling. *Cell Signal* **2021**, *80*, 109929. DOI: 10.1016/j.cellsig.2021.109929 From NLM.
(34) Nguyen, D. H.; Taub, D. Cholesterol is essential for macrophage inflammatory protein 1 beta binding and conformational integrity of CC chemokine receptor 5. *Blood* **2002**, *99* (12), 4298-4306. DOI: 10.1182/blood-2001-11-0087 From NLM.
(35) Luo, N.; Weber, J. K.; Wang, S.; Luan, B.; Yue, H.; Xi, X.; Du, J.; Yang, Z.; Wei, W.; Zhou, R.; et al. PEGylated graphene oxide elicits strong immunological responses despite surface passivation. *Nat Commun* **2017**, *8*, 14537. From NLM.
(36) Gu, Z.; Chen, S. H.; Ding, Z.; Song, W.; Wei, W.; Liu, S.; Ma, G.; Zhou, R. The molecular mechanism of robust macrophage immune responses induced by PEGylated molybdenum disulfide. *Nanoscale* **2019**, *11* (46), 22293-22304. DOI: 10.1039/c9nr04358f From NLM.
(37) Silva Filho, F. C.; Santos, A. B.; de Carvalho, T. M.; de Souza, W. Surface charge of resident, elicited, and activated mouse peritoneal macrophages. *J Leukoc Biol* **1987**, *41* (2), 143-149. DOI: 10.1002/jlb.41.2.143 From NLM.
(38) Chakraborty, P.; Dipankar, P.; Dash, S. P.; Priya; Srivastava, S.; Dhyani, R.; Navani, N. K.; Sharma, D.; Sarangi, P. P. Electrostatic Surface Potential of Macrophages Correlates with Their Functional Phenotype. *Inflammation* **2020**, *43* (2), 641-650. DOI: 10.1007/s10753-019-01146-3 From NLM.
(39) Montenegro-Burke, J. R.; Sutton, J. A.; Rogers, L. M.; Milne, G. L.; McLean, J. A.; Aronoff, D. M. Lipid profiling of polarized human monocyte-derived macrophages. *Prostaglandins Other Lipid Mediat* **2016**, *127*, 1-8. DOI: 10.1016/j.prostaglandins.2016.11.002 From NLM.
(40) Morgan, P. K.; Huynh, K.; Pernes, G.; Miotto, P. M.; Mellett, N. A.; Giles, C.; Meikle, P. J.; Murphy, A. J.; Lancaster, G. I. Macrophage polarization state affects lipid composition and the channeling of exogenous fatty acids into endogenous lipid pools. *J Biol Chem* **2021**, *297* (6), 101341. DOI: 10.1016/j.jbc.2021.101341 From NLM.
(41) Verkleij, A. J.; Zwaal, R. F.; Roelofsen, B.; Comfurius, P.; Kastelijn, D.; van Deenen, L. L. The asymmetric distribution of phospholipids in the human red cell membrane. A combined study using phospholipases and freeze-etch electron microscopy. *Biochim Biophys Acta* **1973**, *323* (2), 178-193. DOI: 10.1016/0005-2736(73)90143-0 From NLM.
(42) Stillwell, W. Chapter 5 - Membrane Polar Lipids. In *An Introduction to Biological Membranes (Second Edition)*, Elsevier, 2016; pp 63-87.
(43) van Duyl, B. Y.; Ganchev, D.; Chupin, V.; de Kruijff, B.; Killian, J. A. Sphingomyelin is much more effective than saturated phosphatidylcholine in excluding unsaturated phosphatidylcholine from domains formed with cholesterol. *FEBS Lett* **2003**, *547* (1-3), 101-106. DOI: 10.1016/s0014-5793(03)00678-1 From NLM.
(44) Lönnfors, M.; Doux, J. P.; Killian, J. A.; Nyholm, T. K.; Slotte, J. P. Sterols have higher affinity for sphingomyelin than for phosphatidylcholine bilayers even at equal acyl-chain order. *Biophys J* **2011**, *100* (11), 2633-2641. From NLM.
(45) Bera, I.; Klauda, J. B. Molecular Simulations of Mixed Lipid Bilayers with Sphingomyelin, Glycerophospholipids, and Cholesterol. *J Phys Chem B* **2017**, *121* (20), 5197-5208. DOI: 10.1021/acs.jpcb.7b00359 From NLM.

(46) Dai, L.; Bhargava, P.; Stanya, K. J.; Alexander, R. K.; Liou, Y. H.; Jacobi, D.; Knudsen, N. H.; Hyde, A.; Gangl, M. R.; Liu, S.; et al. Macrophage alternative activation confers protection against lipotoxicity-induced cell death. *Mol Metab* **2017**, *6* (10), 1186-1197. DOI: 10.1016/j.molmet.2017.08.001 From NLM.
(47) Yu, F.; Yu, N.; Peng, J.; Zhao, Y.; Zhang, L.; Wang, X.; Xu, X.; Zhou, J.; Wang, F. Emodin inhibits lipid accumulation and inflammation in adipose tissue of high-fat diet-fed mice by inducing M2 polarization of adipose tissue macrophages. *Faseb j* **2021**, *35* (7), e21730. DOI: 10.1096/fj.202100157RR From NLM.
(48) Prieur, X.; Mok, C. Y.; Velagapudi, V. R.; Núñez, V.; Fuentes, L.; Montaner, D.; Ishikawa, K.; Camacho, A.; Barbarroja, N.; O'Rahilly, S.; et al. Differential lipid partitioning between adipocytes and tissue macrophages modulates macrophage lipotoxicity and M2/M1 polarization in obese mice. *Diabetes* **2011**, *60* (3), 797-809. DOI: 10.2337/db10-0705 From NLM.
(49) Rubio, J. M.; Astudillo, A. M.; Casas, J.; Balboa, M. A.; Balsinde, J. Regulation of Phagocytosis in Macrophages by Membrane Ethanolamine Plasmalogens. *Front Immunol* **2018**, *9*, 1723. DOI: 10.3389/fimmu.2018.01723 From NLM.
(50) Tierney, J. B.; Kharkrang, M.; La Flamme, A. C. Type II-activated macrophages suppress the development of experimental autoimmune encephalomyelitis. *Immunol Cell Biol* **2009**, *87* (3), 235-240. DOI: 10.1038/icb.2008.99 From NLM.
(51) Denney, L.; Kok, W. L.; Cole, S. L.; Sanderson, S.; McMichael, A. J.; Ho, L. P. Activation of invariant NKT cells in early phase of experimental autoimmune encephalomyelitis results in differentiation of Ly6Chi inflammatory monocyte to M2 macrophages and improved outcome. *J Immunol* **2012**, *189* (2), 551-557. DOI: 10.4049/jimmunol.1103608 From NLM.
(52) Atri, C.; Guerfali, F. Z.; Laouini, D. Role of Human Macrophage Polarization in Inflammation during Infectious Diseases. *Int J Mol Sci* **2018**, *19* (6). From NLM.
(53) Petkevicius, K.; Virtue, S.; Bidault, G.; Jenkins, B.; Çubuk, C.; Morgantini, C.; Aouadi, M.; Dopazo, J.; Serlie, M. J.; Koulman, A.; et al. Accelerated phosphatidylcholine turnover in macrophages promotes adipose tissue inflammation in obesity. *Elife* **2019**, *8*. DOI: 10.7554/eLife.47990 From NLM.
(54) Gaus, K.; Rodriguez, M.; Ruberu, K. R.; Gelissen, I.; Sloane, T. M.; Kritharides, L.; Jessup, W. Domain-specific lipid distribution in macrophage plasma membranes. *J Lipid Res* **2005**, *46* (7), 1526-1538. DOI: 10.1194/jlr.M500103-JLR200 From NLM.